

FUNDAMENTAL ANALYSIS OF SURFACE ACOUSTIC WAVE PROPAGATION

E. LANGER

Institute for Microelectronics, Technical University of Vienna, Gusshausstrasse 27-29/360, A-1040
Wien, Austria

Abstract—Numerical techniques for the analysis and simulation of surface acoustic wave generation and propagation are presented. The first part of this contribution deals with a numerical algorithm for the extraction of SAW properties with respect to different substrate materials and arbitrary crystal cuts. As one particular application this algorithm is used to improve the accuracy of the tensor coefficients of the substrate material LiNbO_3 . The second part concerns a two-dimensional transient simulation of acoustic wave generation by interdigital transducers. The developed simulation tool is applied to investigations about parasitic bulk wave generation. Finally, some remarks on the computational requirements are given.

1. INTRODUCTION

Modeling of wave propagation phenomena in anisotropic piezoelectric materials has become eminently important for surface acoustic wave device characterization and design. Most of the common computer programs for the analysis of the extrinsic device behavior require on input the phase velocity of the surface wave [9], and in many cases the decay of the surface wave into the bulk is also of great interest. As experimental results are difficult to obtain for arbitrary crystal cuts the developed efficient algorithm for the calculation of the properties of surface acoustic waves (Section 3) is an important tool for the investigation of less common materials and crystal cuts.

One concrete application presented in this paper (Section 4) concerns the improvement of material data using measured SAW velocities and a nonlinear least squares algorithm that needs as basis a fast algorithm for computing the SAW velocities at given tensor coefficients.

In contrast to the above mentioned question for the properties of theoretically undamped propagating surface acoustic waves the developed two-dimensional, transient simulation program takes also a given stimulation by an interdigital transducer as well as the resulting second-order effects (i.e. bulk wave generation and interaction between bulk and surface waves) into account (Section 5). That program solves the initial boundary value problem (with "artificial boundaries") time-dependent by a semi-implicit finite difference scheme. It is worthwhile to note that the tensor coefficients for the most common materials and used by both programs are stored in a database where new materials can easily be added. Furthermore, any arbitrary crystal cut defined by the so-called Euler's angles [13] can be analyzed.

2. PHYSICAL MODEL

The physical model is based on the fundamental set of equations describing acoustic wave propagation in arbitrary piezoelectric material consisting of equations of motion (1), the linear, strain-mechanical displacement relations (2), Maxwell's equation under the quasi-static assumptions (3), (4) and the linear piezoelectric constitutive relations (5), (6) [2]. It is to be noted that standard tensor notation as well as Einstein's summation convention is used.

$$\frac{\partial T_{ij}}{\partial x_i} = \rho \cdot \frac{\partial^2 u_j}{\partial t^2} \quad (1)$$

$$S_{km} = \frac{1}{2} \cdot \left(\frac{\partial u_k}{\partial x_m} + \frac{\partial u_m}{\partial x_k} \right) \quad (2)$$

$$\frac{\partial D_i}{\partial x_i} = 0 \quad (3)$$

$$E_i = -\frac{\partial \phi}{\partial x_i} \quad (4)$$

$$T_{ij} = c_{ijkl} \cdot S_{km} - e_{nij} \cdot E_n \quad (5)$$

$$D_i = e_{ikm} \cdot S_{km} + \varepsilon_{in} \cdot E_n \quad (6)$$

T denotes the stress, ρ the mass density, u the mechanical displacement, S the strain, D the electric displacement, E the electric field, ϕ the electric potential. The fourth rank tensor c is the elastic stiffness tensor, the third rank tensor e the piezoelectric tensor, and the second rank tensor ε the dielectric tensor in the actual, i.e. rotated according to the given Euler's angles, coordinate system.

By substituting equations (2) and (4) into equations (5) and (6) and then eliminating the mechanical stress T and the electric displacement D , one obtains a system of partial differential equations in three spatial dimensions ($j = 1, 2, 3$) which consists of three mechanical wave equations (7) and Poisson's equation (8):

$$c_{ijkl} \cdot \frac{\partial^2 u_k}{\partial x_i \partial x_m} + e_{nij} \cdot \frac{\partial^2 \phi}{\partial x_i \partial x_n} = \rho \cdot \frac{\partial^2 u_j}{\partial t^2} \quad (7)$$

$$e_{ikm} \cdot \frac{\partial^2 u_k}{\partial x_i \partial x_m} - \varepsilon_{in} \cdot \frac{\partial^2 \phi}{\partial x_i \partial x_n} = 0 \quad (8)$$

For all following considerations the system is reduced to two spatial dimensions $x = x_1$ and $z = x_3$, i.e. the sagittal plane (x denotes the SAW propagation direction and z is perpendicular to the surface) assuming negligible derivatives of all parameters in direction $y = x_2$ which is perpendicular to the sagittal plane.

This is no restriction at all for the analysis of the exact surface acoustic waves since plane waves are assumed in that case. For the two-dimensional time-dependent simulation that assumption means that the finger length of the interdigital transducer structure must be infinite or—more realistic—at least much larger than the finger width.

Defining the solution vector \mathbf{s} with its components u_1, u_2, u_3 (components of the mechanical displacement vector \mathbf{u}) and ϕ (electrical potential) leads to the following matrix equation (9):

$$A \cdot \mathbf{s}_{xx} + B \cdot \mathbf{s}_{xz} + C \cdot \mathbf{s}_{zz} = \Omega \cdot \mathbf{s}_u \quad (9)$$

A, B, C , and Ω are symmetric 4×4 matrices where Ω is a diagonal matrix whose main diagonal has the entries $\rho, \rho, \rho, 0$. The elements of A, B , and C consist without exception of the coefficients of the material tensors c, e , and ε . As the values of the elastic stiffness tensor c and of the dielectric tensor ε are in the order of 10^{10} and 10^{-10} , respectively, the scaling of the equation system is an absolute necessity for all numerical investigations. Owing to lack of space the adequate scaling procedure can not be discussed here in detail.

3. ANALYSIS OF SAW PROPERTIES

This section deals with a description of a recently developed algorithm for an efficient computation of surface acoustic wave properties for arbitrary propagation directions. In contrast to an early publication [7] the SAW solution is derived here from the functional relationship between the so-called "effective permittivity" (10) and the phase velocity [10]. There are two reasons for this modification: on the one hand the new algorithm is faster and on the other hand more stable even for propagation directions with weak piezoelectric coupling since the effective permittivity is a physical quantity that describes the electrical material properties on the surface with respect to wave propagation.

$$\varepsilon_{\text{eff}} = \frac{\sigma}{|k| \cdot \phi} \quad \text{for } z = 0 \quad (10)$$

The formula for the effective permittivity includes the plane charge σ at the surface, the wave number k , and the electric potential ϕ at the surface. It can easily be seen that this formula includes two special cases of electrical boundary conditions: $\sigma=0$ means the boundary condition for a free surface (ϵ_{eff} is singular) and $\phi(0)=0$ means a constant and time independent potential at the surface and therefore an ideally metallized surface (ϵ_{eff} has a pole in this case).

The plane charge can be substituted by $\sigma = D_3 - D_a$ where D_3 and D_a are the components of the electric displacement perpendicular to the surface in the substrate material and in the surrounding air, respectively (but both infinitely close to the surface). In order to obtain only variables defined within the substrate one has to eliminate D_a by solving the Laplace equation in the air (11):

$$\Delta \phi_a = 0 \quad (11)$$

My model of the surface wave is a linear combination of partial waves (12). In contrast to other authors I do not assume a pure exponential decay of these partial waves into the depth but allow a general vector function $\mathbf{g}(z)$.

$$\mathbf{s} = \exp(jkx - j\omega t) \cdot \mathbf{g}(z) \quad (12)$$

Substituting (12) into Laplace equation (11) leads to

$$g_a = a_1 \cdot e^{|k|z} + a_2 \cdot e^{-|k|z}, \quad (13)$$

where the constant a_1 must vanish because the limit of $g_a(z)$ for $z \rightarrow +\infty$ has to be zero. a_2 is estimated by a comparison of g_a with g_4 for $z = 0$ ($a_2 = \phi(0)$) and one obtains

$$D_a = -\epsilon_0 \cdot \frac{\partial \phi_a}{\partial z} = \epsilon_0 \cdot |k| \cdot \phi \quad \text{for } z = 0. \quad (14)$$

After the elimination of D_a the formula for the effective permittivity (10) can be rewritten as

$$\epsilon_{\text{eff}} = \epsilon_0 \cdot \left[1 - j \cdot \frac{D_3}{jk} \cdot \frac{\text{sign}(k)}{\epsilon_0 \cdot \phi(0)} \right], \quad (15)$$

where the electrical quantities D_3 and $\phi(0)$ must be supplied by the solution of the partial differential equation set (9) in connexion with the mechanical surface boundary condition $T_{3j} = 0$ for $j = 1, 2, 3$ and $z = 0$. That condition results from the fact that all force components perpendicular to the surface have to vanish since the air can not supply a compensating force.

The mechanical boundary condition at the surface yealds the matrix equation (16) where the fourth equation is no (electrical) boundary condition at all but finally necessary for the computation of D_3 which is needed for the effective permittivity (15).

$$B_0 \cdot \mathbf{s}_x + C \cdot \mathbf{s}_z = (0, 0, 0, D_3)^T \quad \text{for } z = 0 \quad (16)$$

It should be mentioned that the relation $B_0 + B_0^T = B$ holds.

It is advantageous to make a transformation of the z -coordinate by introducing the new function \mathbf{f} according to $\mathbf{g}(z) = \mathbf{f}(\xi) = \mathbf{f}(j|k|z)$. Substituting the SAW model (12) into equations (9) and (16) yealds a homogeneous system of four ordinary differential equations (17) with the phase velocity $v = \omega/k$ as parameter and the mechanical surface boundary condition (18).

$$(A - v^2 \cdot \Omega) \cdot \mathbf{f} + \text{sign}(k) \cdot B \cdot \mathbf{f}' + C \cdot \mathbf{f}'' = 0 \quad (17)$$

$$B_0 \cdot \mathbf{f} + \text{sign}(k) \cdot C \cdot \mathbf{f}' = (0, 0, 0, D_3/(jk))^T \quad \text{for } \xi = 0 \quad (18)$$

As the solution must decrease in depth direction the trivial boundary condition $\mathbf{s}(x, \xi, t) = 0$ for $\xi \rightarrow -j \cdot \infty$ holds. To solve the second order ordinary differential equation system (17) it is transformed to first order (20) using the new solution vector \mathbf{h} (19).

$$\mathbf{h}_1 = \mathbf{f}, \quad \mathbf{h}_2 = B_0 \cdot \mathbf{f} + \text{sign}(k) \cdot C \cdot \mathbf{f}' \quad (19)$$

$$\mathbf{h}' = H \cdot \mathbf{h} \quad \text{with} \quad H = \text{sign}(k) \cdot \begin{pmatrix} -C^{-1} \cdot B_0 & C^{-1} \\ v^2 \cdot \Omega - A + B_0^T \cdot C^{-1} \cdot B_0 & -B_0^T \cdot C^{-1} \end{pmatrix} \quad (20)$$

The formal solution reads

$$\mathbf{h} = G \cdot \exp(\Lambda \cdot \xi) \cdot \boldsymbol{\eta}, \tag{21}$$

where G denotes the eigenvector matrix of H , Λ is a diagonal matrix whose entries are the eigenvalues of H , and $\boldsymbol{\eta}$ is a linear combination vector representing the amplitudes of the partial waves. If one reorders the eigenvalues within Λ (and, of course, also the eigenvectors within G) in that way that the first four represent decreasing solutions in depth direction (i.e. these eigenvalues must have a negative imaginary part) one can set the last four components of $\boldsymbol{\eta}$ to zero, thus eliminating the unphysically increasing solutions. The other components of $\boldsymbol{\eta}$ are obtained by solving the linear homogeneous algebraic equation system (22) where $\boldsymbol{\eta}_1$ denotes the first four components of $\boldsymbol{\eta}$.

$$\mathbf{h}_2^* = G_{21}^* \cdot \boldsymbol{\eta}_1 = 0 \quad \text{for} \quad \xi = 0 \tag{22}$$

This equation results from the substitution (19) where the left side of the mechanical boundary condition (18) has been used. G_{21} represents the lower left 4×4 submatrix of G ; the superscript “*” in equation (22) means that the fourth component of \mathbf{h}_2 and the fourth row of G_{21} , respectively, has to be ignored.

Now it is possible to calculate the effective permittivity (15) for a given phase velocity v : $D_3/(jk)$ is given by the fourth row of the left side of equation (18) and therefore by the last row of the solution for \mathbf{h} (21) with $\xi = 0$; the surface potential is given by the fourth component of \mathbf{h} with $\xi = 0$. This procedure leads to the final expression for the normalized effective permittivity:

$$\frac{\epsilon_{\text{eff}}}{\epsilon_0} = 1 - j \cdot \text{sign}(k) \cdot \frac{\sum_{i=1}^4 G_{8i} \cdot \eta_i}{\epsilon_0 \cdot \sum_{i=1}^4 G_{4i} \cdot \eta_i} \tag{23}$$

If that expression is zero or quasi infinite the undamped propagating SAW for the given propagation direction has been found and its depth dependence is given by

$$\mathbf{g}(z) = \sum_{i=1}^4 (\mathbf{G}_{11})_i \cdot \eta_i \cdot \exp(\lambda_i \cdot j |k| z), \tag{24}$$

where $(\mathbf{G}_{11})_i$ represents the i th column of the submatrix G_{11} and λ_i is the corresponding eigenvalue of H .

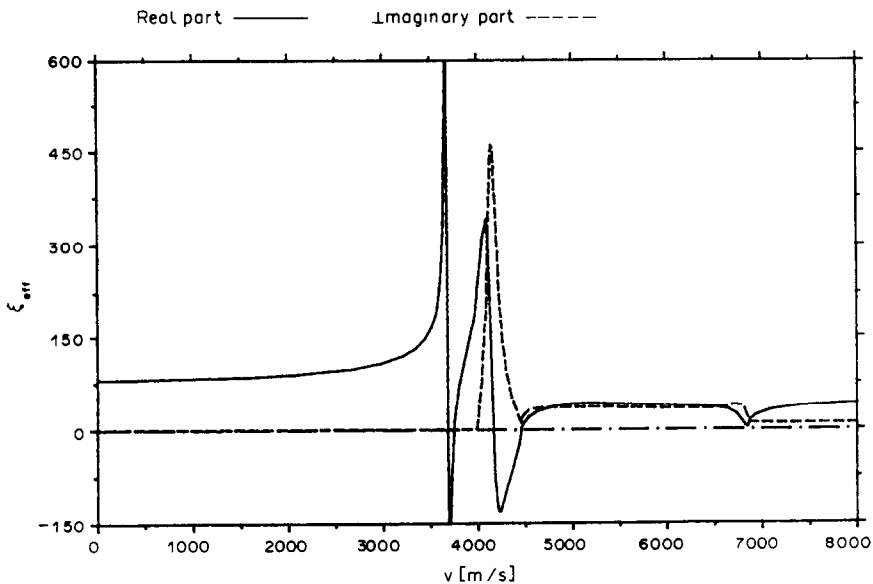


Fig. 1. Typical behavior of the effective permittivity.

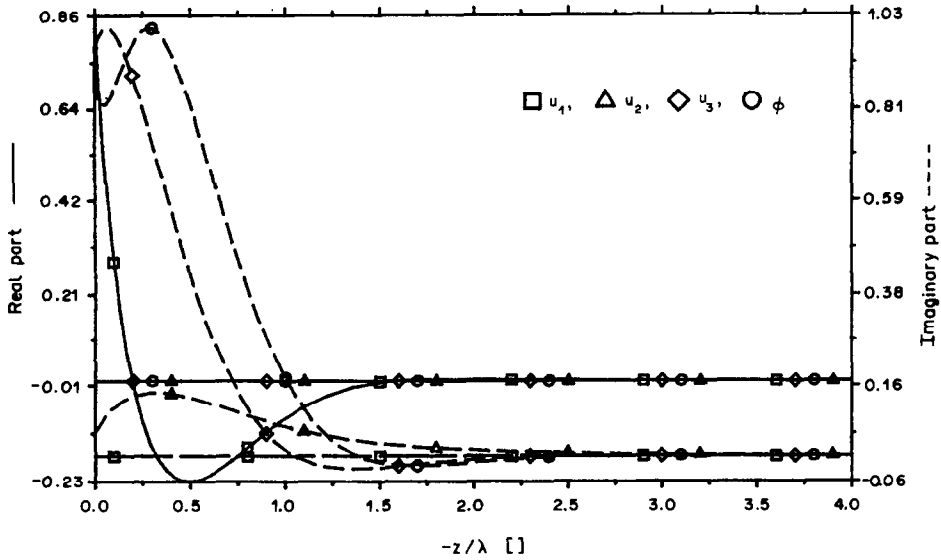


Fig. 2. Decay into depth of SAW for 128° rotated Y-LiNbO₃.

Figure 1 shows the typical behavior of the normalized effective permittivity depending on the phase velocity for Lithiumniobate with Euler's angles $\lambda = 90^\circ$, $\mu = 90^\circ$, and $\Theta = 0^\circ$. One can see that ϵ_{eff} is a monotonously increasing real function for low velocities until it reaches the pole where the solution of the SAW-problem for the metallized surface is located. After the pole it is increasing again and passes zero where the free surface solution can be found. Beginning at a certain phase velocity the effective permittivity becomes complex.

This behavior of the functional relationship between the effective permittivity and the phase velocity offers an easily implementable searching algorithm: starting with a velocity which is certainly higher than the SAW-velocity for the free surface (e.g. the velocity of the slower transversal bulk mode) one has to calculate ϵ_{eff} with decreasing velocity until the singularity and/or the pole has been found.

The solution vector $\mathbf{g}(z)$ with its four components u_1 , u_2 , u_3 , and ϕ is shown in Fig. 2 for the 128° rotated Y-cut of LiNbO₃ (free surface). The full lines represent the real part and the

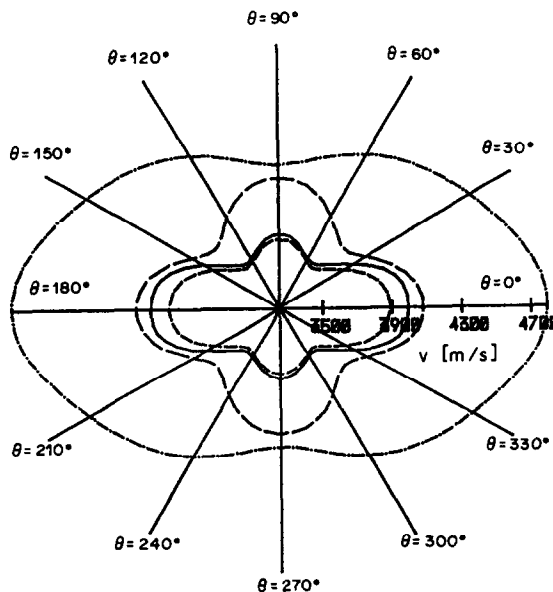


Fig. 3. Phase velocities in the surface of 128° rotated Y-LiNbO₃.

dashed lines the imaginary part; the length of the displacement vector \mathbf{u} at the surface has been normalized to 1. One can nicely observe that the surface acoustic wave is nearly vanishing within two wavelength for that special crystal cut of LiNbO_3 . It should also be mentioned that there is a constant phase shift of 90° between the component u_1 (which has no imaginary part) and the other components u_2 , u_3 , and ϕ (whose real part is zero). The maximum value of the component u_2 —the displacement component perpendicular to the sagittal plane—is significantly smaller than the other components of \mathbf{u} .

Figure 3 shows the phase velocities in the surface of the 128° rotated Y-cut of LiNbO_3 : the full line and the short dashed line correspond to the SAW velocities for the free and the metallized surface, respectively. Furthermore, one can see on this drawing the phase velocities of the bulk transversal modes propagatable parallel to the surface (but within the crystal volume). The origin of Fig. 3 corresponds to a phase velocity of 3250 m/s. Just such a plot allows to select the most useful propagation direction for a possible surface acoustic wave device: for $\Theta = 0$ the piezoelectric coupling (that is proportional to the difference between the two SAW velocities) has a maximum and the partial derivative $\partial v / \partial \Theta$ has a minimum what is very important for the reproducibility of surface acoustic devices.

4. IMPROVEMENT OF MATERIAL DATA OF LiNbO_3

In the past, several authors, e.g. [15], [14], [11], [3], made careful experiments to determine either a complete data set or some specific constants of LiNbO_3 where the techniques used are based on bulk acoustic wave propagation. Additional low frequency capacity measurements are mostly included. However, even for this widely investigated material the derived and published constants typically vary from some percent up to 10%. As an example Table 1 compares the 13 independent constants of LiNbO_3 as found by (a) Warner *et al.* [15], (b) Smith and Welsh [14], and (c) Nakagawa *et al.* [11]. The superscripts E and S mean measurements at constant electric field and constant strain, respectively; abbreviated notation for c_{ij}^E and e_{ij}^S is assumed, as usually. Figure 4 shows a comparison of the SAW velocities measured by Anhorn *et al.* [1] (full line) for free surface with the calculated data given in Table 1 (dashed line: Warner *et al.*, dotted line: Smith and Welsh, dashed-dotted line: Nakagawa *et al.*). While the data by Nakagawa *et al.* give the best overall agreement the velocity for the Z-axis is met best by Warner *et al.* However, in all three cases the average velocity difference is much more than the measurement accuracy of 1 m/s as it can be seen in the lower part of Fig. 4.

Our aim was now to fit optimally the material constants of LiNbO_3 to the measured SAW velocities; that has been achieved by using a nonlinear least squares algorithm. As this algorithm can not be discussed here in detail the interested reader is referred to [6]. This method can be extended in quite a straight forward way to include other measurements, too. There are only two requirements to add further equations: (1) an accurate measurement as well as a good estimate of it's accuracy and (2) a (nonlinear) model to calculate the measured quantity as a function of the unknown crystal constants.

Table 1. Independent constants for LiNbO_3

	(a)	(b)	(c)
ρ [10 ³ kg/m ³]	4.7	4.64	4.7
c_{11}^E [10 ¹⁰ N/m ²]	20.3	20.30	20.0
c_{12}^E [10 ⁹ N/m ²]	5.3	5.73	5.4
c_{13}^E [10 ⁹ N/m ²]	7.5	7.52	6.0
c_{14}^E [10 ⁹ N/m ²]	0.9	0.85	0.8
c_{33}^E [10 ⁹ N/m ²]	24.5	24.24	24.3
c_{44}^E [10 ⁹ N/m ²]	6.0	5.95	6.0
e_{15} [C/m ²]	3.7	3.76	3.8
e_{22} [C/m ²]	2.5	2.43	2.5
e_{31} [C/m ²]	0.2	0.23	0.35
e_{33} [C/m ²]	1.3	1.33	1.42
ϵ_{11}^S [ϵ_0]	44	44.30	42.72
ϵ_{33}^S [ϵ_0]	29	27.90	27.16

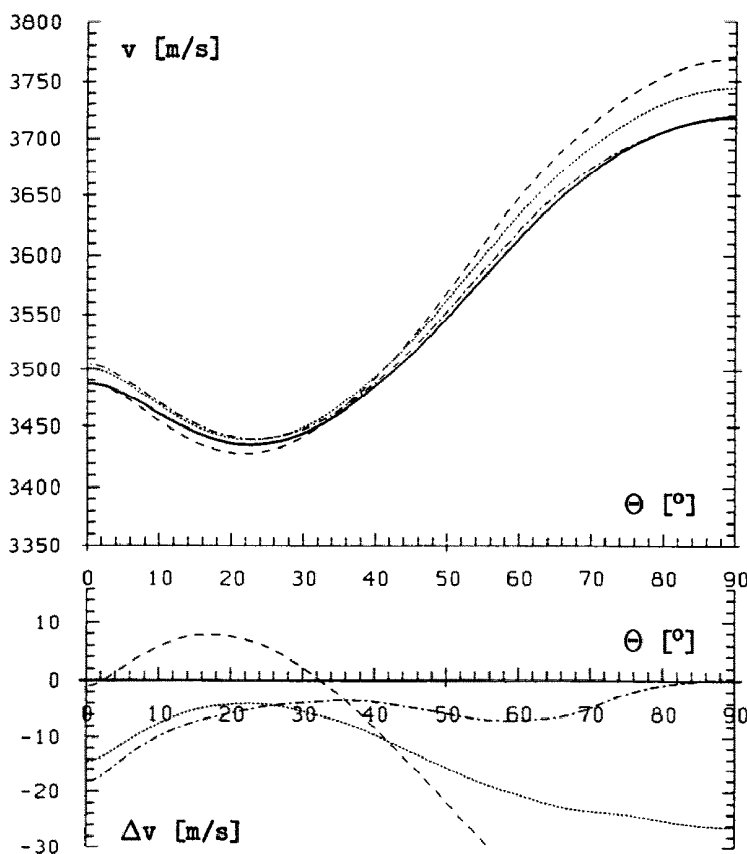


Fig. 4. Free surface SAW velocities on Y-cut LiNbO₃.

For the case of the SAW velocities the measurements are taken from Anhorn *et al.* [1] and the mathematical model is based on the calculation of the SAW velocities described already in Section 3. From our first calculations we have realized that it is not possible to obtain all 13 independent materials constants of LiNbO₃ from SAW velocity measurements only. This can easily be understood from the following equations:

$$v_{\text{SAW}} \sim f\left(\sqrt{\frac{\bar{c}}{\rho}}\right), \quad \bar{c} = c + \frac{e^2}{\varepsilon} \quad (25)$$

Scaling of the complete data set with an arbitrary constant results in almost the same SAW velocities, and there are even additional degrees of freedom because only the ratio of e^2 to ε gives the piezoelectric stiffening of c . As a consequence of this discussion we have included in addition to the measured SAW velocities equations for the definition of the mass density ρ and the dielectric tensor ε within a reasonable interval.

Surprisingly even for such a basic parameter as the mass density the published values vary from 4628 kg/m³ to 4700 kg/m³ at room temperature. This may partly be explained by the fact that commercially available LiNbO₃ has changed over the years [5]. An accurate measurement of the mass density, therefore, is strongly recommended.

Figure 5 represents the velocity difference for Y-cut LiNbO₃ between the measurements by Anhorn *et al.* and the curves calculated from our fitted constants (full line: free surface, dotted line: metallized surface). The maximum deviation is less than 1.2 m/s and the average is about 0.43 m/s. While most constants obtained from our calculations are roughly within the range of those from Table 1, the piezoelectric constant e_{33} is distinctly greater and, as a consequence, c_{33}^E is smaller. Our result is most similar to the value found by Graham [4] who measured the piezoelectric stress constants from shock wave propagation.

It should be noted that the accuracy of the obtained tensor coefficients does not depend only on the accuracy of the measured velocities but also on the crystal cut chosen for the

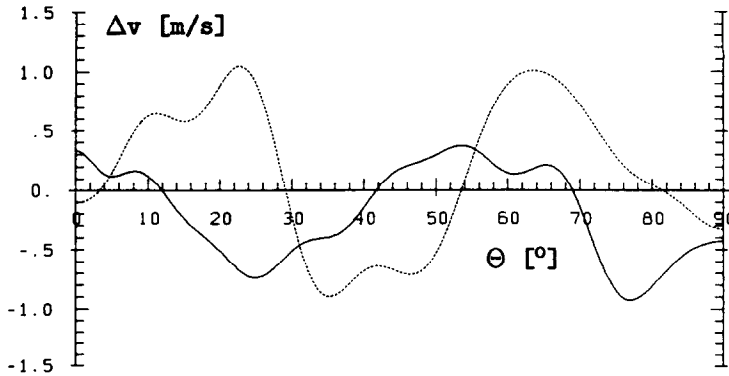


Fig. 5. Difference between measured and calculated SAW velocities based on fitted tensor coefficients.

measurements. While the measurements on Y-cut LiNbO_3 provide not enough information to reach high precision, the SAW velocities on 128° rotated Y- LiNbO_3 are sensitive to all material constants.

5. TWO-DIMENSIONAL TRANSIENT SIMULATION

As already reported in Section 2 the investigations of the time-dependent simulation of surface acoustic wave generation and propagation are restricted to the two spatial dimensions in the sagittal plane. The primary reason for this is actually the enormous amount of computing resources required by a three-dimensional numerical solution of the partial differential equation set (7), (8). Such an expense is not necessary as I am mainly interested in the parasitic bulk wave generation of interdigital transducers. Figure 6 shows the geometry of the investigated transducer structures schematically. The length of the metallized fingers in y -direction is assumed to be much larger than the finger width.

The second order partial differential equation system (9) to be solved as well as the surface boundary condition for the free parts of the surface (16) are the same as in Section 3 whereas the surface boundary condition at the electrodes is given by

$$B_m \cdot s_x + C_m \cdot s_z + M_m \cdot s = (0, 0, 0, \phi_k)^T. \quad (26)$$

This “mixed” boundary condition results from the Neumann conditions for the mechanical wave equations and from the Dirichlet condition for the electric potential. Assuming negligible mass loading of the electrodes the first three rows of B_m and C_m are equal to the corresponding rows of B_0 and C and the fourth row of B_m and C_m is zero. The matrix M_m has only one non-zero entry (the element 44).

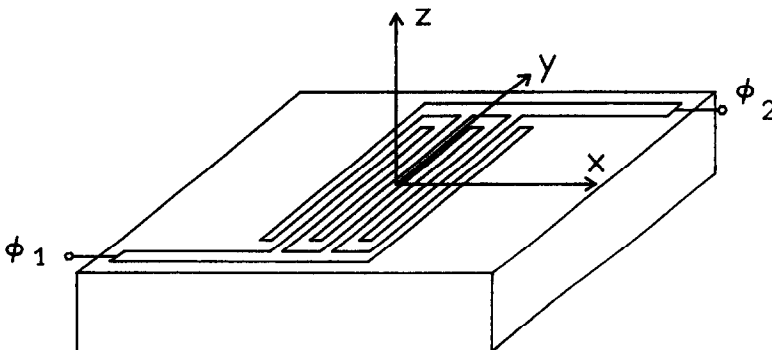


Fig. 6. Principle geometry of a transducer structure.

The most serious problem is represented by all other boundaries as it is not yet applicable to simulate a whole SAW device because of the two following reasons: (1) the dimensions of real devices would lead to an equation system of extremely high rank after the discretization, and (2) the practical fabrication of SAW devices includes some special treatment of the bulk boundaries (e.g. sticking on of some viscous material) such that undesired modes are absorbed or at least scattered; these technological steps can not be formulated satisfactory.

Therefore, ignoring the real dimensions and assuming the substrate to build an infinite half-plane one has to introduce artificial boundaries in the sagittal plane in order to obtain a finite-dimensional linear system of equations with (9) and discretized boundary conditions at the surface (16), (26) for each timestep. The obvious way to do this is to solve the problem in a rectangle (which includes all fingers) and to impose zero Neumann or Dirichlet boundary conditions at those boundaries of the rectangle which do not coincide with the surface. This approach, however, leads to reflections as soon as the first wave (i.e. in general a longitudinal bulk mode) hits the artificial boundary and, therefore, has to be abandoned. The method of transformation of the infinite sagittal plane into finite subdomains [8] has the drawback of relatively large discretization errors in these domains.

My actually preferred method is based on the fact that at a sufficiently large distance from the fingers there exist mainly plane bulk waves with approximately radial propagation direction. First equation (9) is transformed into polar coordinates r , α and the limiting value for r to infinity is formed. This yields a system of partial differential equations in one spatial dimension which has the mentioned plane waves as solutions:

$$Q \cdot s_{rr} = \Omega \cdot s_{\alpha\alpha} \quad \text{with} \quad Q = A \cdot \cos^2 \alpha + B \cdot \sin \alpha \cdot \cos \alpha + C \cdot \sin^2 \alpha \quad (27)$$

The boundary condition (28) which is a generalized form of Sommerfeld's radiation condition, satisfies the equation system (9) implicitly and, therefore, absorbs all possible radial propagating plane waves.

$$s_r = s_x \cdot \cos \alpha + s_z \cdot \sin \alpha = -\sqrt{Q(\alpha)^{-1} \Omega} \cdot s_t \quad (28)$$

The discretization is performed by the finite difference method with an equidistant spatial mesh and a constant time step size. The grid spacing depends, of course, on the required resolution concerning the electrodes as well as the shortest expected wavelength. In order to get a stable algorithm the criterion

$$\frac{\Delta x}{\Delta t} > \sqrt{\frac{r(A^*) + r(C^*)}{\rho}} \quad (29)$$

must hold [12] where $r(A^*)$ and $r(C^*)$ denote the spectral radii of the 3×3 main minors of A and C (these submatrices only consist of elements of the elastic stiffness tensor). The stability condition (29) forces the algorithm to be "quicker" than the fastest acoustic wave.

Owing to the hyperbolic-elliptic type of the partial differential equation set (7), (8) a semi-implicit time integration scheme must be used for the solution: while the mechanical quantities within the simulation area (i.e. the components of the displacement vector \mathbf{u}) can be calculated for each time step explicitly using the results from the two previous time steps, the electric potential as well as all unknowns at the boundaries build an algebraic equation system (whose rank is given approximately by the number of nodes) which has to be solved at each time step simultaneously.

For the solution of the resulting sparse linear (or linearized) algebraic equation system two different solvers have been implemented: the solution is performed either by Gaussian elimination or iteratively by a modified SOR-algorithm with adaptive relaxation parameter. The choice depends on the number of nodes as well as on the size of the time interval which shall be simulated.

The main advantage of the described finite difference method compared to the frequently used Fourier transform method is that the difference method can easily be applied to non-linear elasticity laws, while the Fourier method relies strictly on the linearity of the problem.

As one particular example I present a transient analysis of a six finger transducer structure for Y-cut Z-propagating LiNbO_3 . The geometry of the simulation area (in the sagittal plane) is

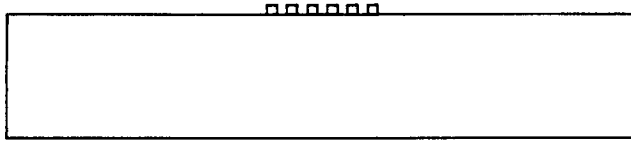


Fig. 7. Geometry of an investigated transducer structure.

shown in Fig. 7. The distance between two neighbouring electrodes as well as the finger width amounts of $21.8 \mu\text{m}$; as I take a so-called $\lambda/4$ -transducer the wavelength of the expected SAW is $87.2 \mu\text{m}$. The dimensions of the simulation area are about 15 wavelength in x -direction and about 3 wavelength into the depth. The resonance frequency of the structure is given by $f = v/\lambda = 40 \text{ MHz}$ since the phase velocity v of the SAW for the actual crystal cut amounts of 3488 m/s .

The applied voltage on the electrodes is a sinusoidal function in time with a horizontal tangent at $t = 0$ to get consistent initial values (all unknowns at $t = 0$ are zero). The amplitude of the voltage is 1 V and the frequency amounts to 40 MHz . Figure 8 shows the mechanical displacement components u_1 (which is the component parallel to the surface) and u_3 (which is perpendicular to the surface) after three periods in a quasi three-dimensional plot. [It should be mentioned that for this special cut of LiNbO_3 , the second equation of the PDE-set (9) is decoupled from the others. Therefore, the mechanical displacement component u_2 is not relevant for wave propagation in this case.] The rectangular bottom of the drawing is the

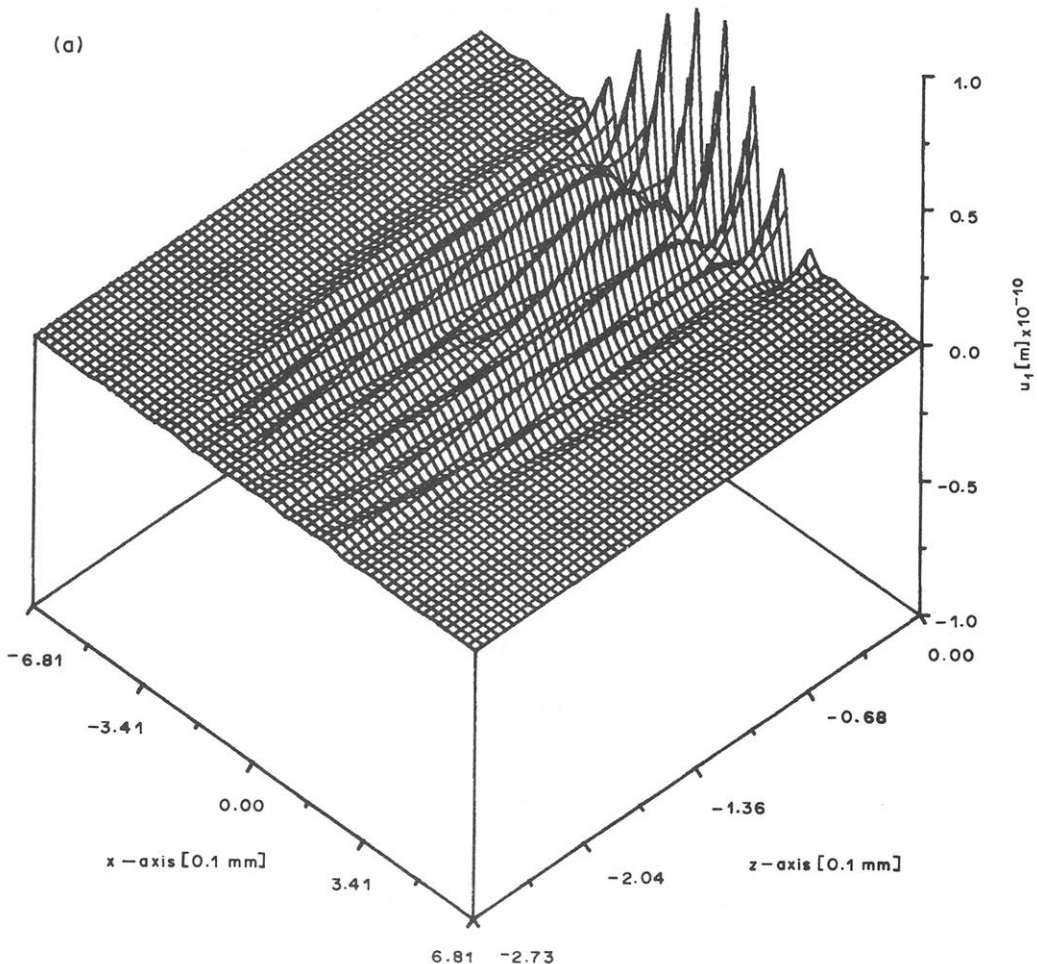


Fig. 8(a). Mechanical displacement component u_1 after three periods.

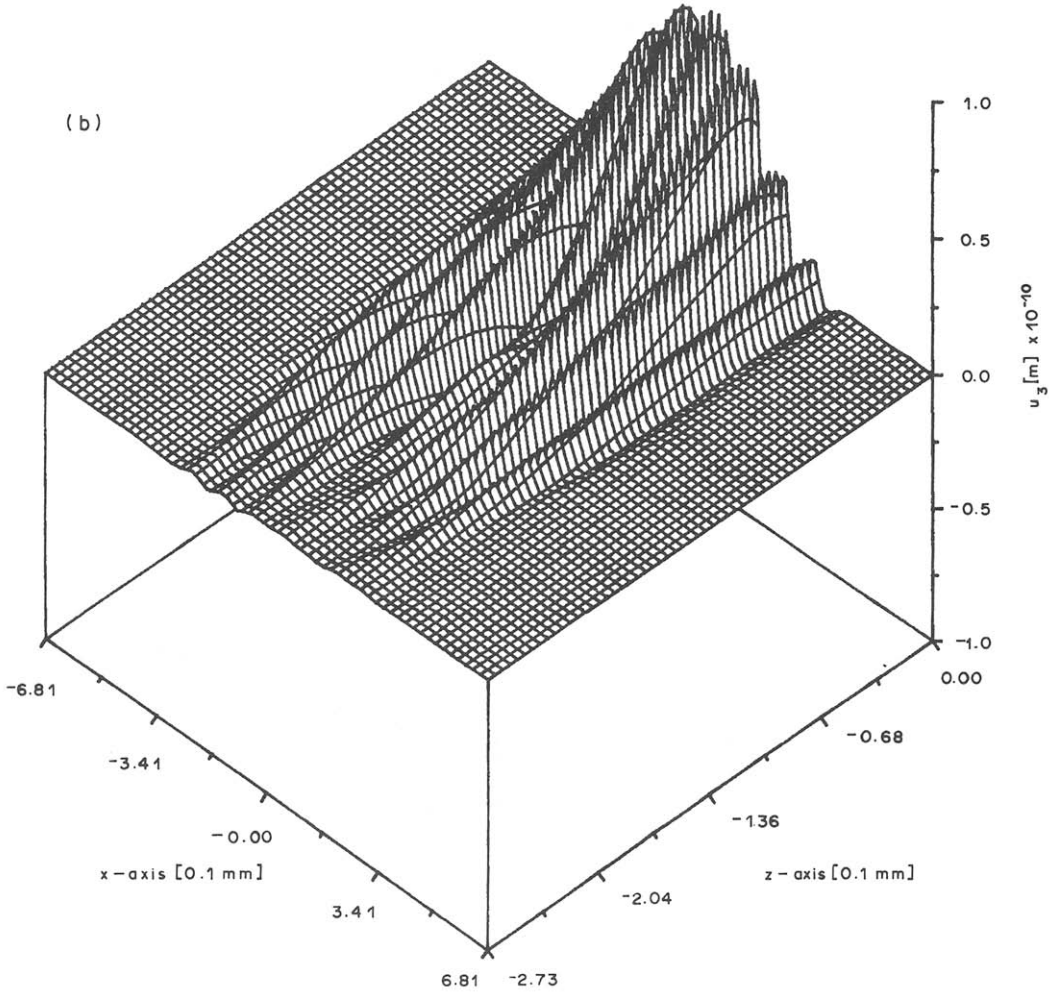


Fig. 8(b). Mechanical displacement component u_3 after three periods.

sagittal plane, whereas the third dimension represents the value of the dependent variable (the scale factor right to the vertical axis amounts to 10^{-10}). Please note that the two axes have been scaled with different factors. The difference of the depth behavior is quite similar to Fig. 2 (although another crystal cut has been analyzed there).

In order to obtain information about the parasitic bulk wave generation the energy radiation of the transducer structure is regarded. For that purpose one has to calculate Poynting's vector \mathbf{P} [2] which represents the transported energy per unit of time and per unit of area. The general Poynting's theorem sounds for the time domain

$$\mathbf{P}(t) = -\mathbf{v}(t) \cdot \mathbf{T}(t) + \mathbf{E}(t) \times \mathbf{H}(t) \quad (30)$$

and in complex notation

$$\mathbf{P} = -\frac{\mathbf{v}^* \cdot \mathbf{T}}{2} + \frac{\mathbf{E} \times \mathbf{H}^*}{2}, \quad (31)$$

where \mathbf{H} denotes the magnetic field and the superscript “*” means the conjugate value. It should be noted that in this context \mathbf{v} represents the particle velocity (i.e. the partial derivative of the displacement vector \mathbf{u} with respect to the time).

Introducing the quasistatic approximation leads to the equations (32) and (33).

$$\mathbf{P}(t) = -\mathbf{v}(t) \cdot \mathbf{T}(t) + \phi(t) \cdot \frac{\partial \mathbf{D}(t)}{\partial t} \quad (32)$$

$$\mathbf{P}_k = -\frac{\mathbf{v}_i^* \cdot \mathbf{T}_{ik}}{2} + \frac{\phi \cdot (j\omega \mathbf{D}_k)^*}{2} \quad (33)$$

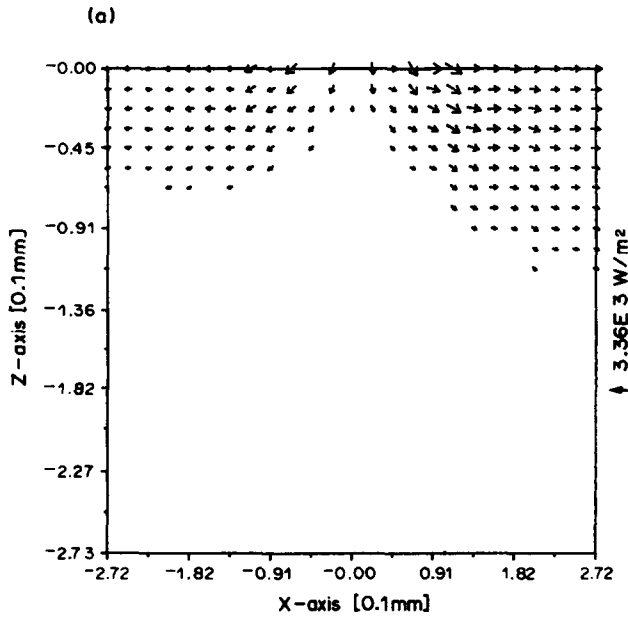


Fig. 9(a). Energy radiation in the sagittal plane.

After substituting equations (3)–(6) into (33) one obtains a formula for the stationary case which only includes the primary variables \mathbf{u} and ϕ :

$$P_k = - \left[\frac{j\omega \cdot \mathbf{u}_i}{2} \right]^* \cdot \left[c_{ikmn} \cdot \frac{\partial u_m}{\partial x_n} + e_{pik} \cdot \frac{\partial \phi}{\partial x_p} \right] + \frac{\phi}{2} \cdot \left[j\omega \cdot \left(e_{kmn} \cdot \frac{\partial u_m}{\partial x_n} - \epsilon_{kp} \cdot \frac{\partial \phi}{\partial x_p} \right) \right]^* \tag{34}$$

Figure 9 shows the real part of Poynting’s vector within two different subdomains of the simulation area. In Fig. 9(a) the vertical dimension is equal to that of the simulation area whereas the size in x-direction is only about one fifth of the investigated geometry in Fig. 7 (it is approximately the area below the electrodes). It can clearly be seen that the energy

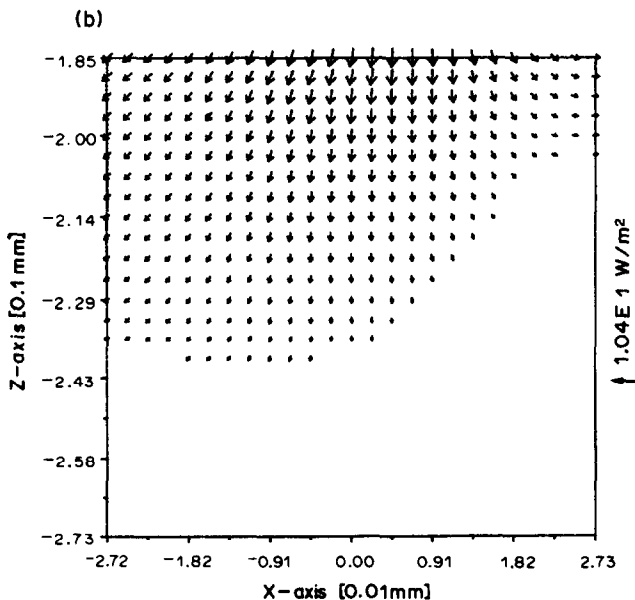


Fig. 9(b). Detailed view of the energy radiation.

radiation for that crystal cut of LiNbO_3 is quite unsymmetric. Most of the transported energy seen in this plot belongs to the generated SAW.

Figure 9(b) represents the distribution of the real part of Poynting's vector within a very small part of the simulation area. Please note that the upper boundary does not represent the surface but the lower boundary is equal to that of the simulation area. The x -dimension is about one tenth of that of Fig. 9(a). This distribution is representative for bulk mode generation as the surface acoustic wave already is very small in such a depth. The information given by the distribution of Poynting's vector now could be processed in order to obtain more quantitative results.

Finally, I should like to give some remarks on the required computational resources of the algorithms briefly described in this paper. The calculation of the two SAW solutions for one propagation direction (Section 3) needs about 2 CP-seconds (the value depends strongly on the starting velocity) on a mainframe computer with 1 million floating point operations per second. This seems not too much, even for the analysis of a wide spectrum of propagation directions within a certain material. For the improvement of the material data (Section 4) some thousands of CP-seconds were necessary. The two-dimensional transient analysis, of course, needs quite a lot of CP-time. The example in this chapter, for instance, requires due to the discretization an estimation of 38403 unknowns per time step and the rank of the sparse linear equation system that has to be solved simultaneously for each time step has a rank of 14001 (the number of grid points in x -direction is 251 and that in z -direction amounts to 51).

Acknowledgment—This work is supported by the research laboratories of Siemens AG at Munich, F.R.G.

REFERENCES

- [1] M. ANHORN, H. E. ENGAN and A. RONNEKLEIV, New SAW velocity measurements on Y-cut LiNbO_3 . In *Ultrasonics Symposium*, 279–284. IEEE (1987).
- [2] B. A. AULD, *Acoustic Fields and Waves in Solids*, Vol. 1. Wiley, New York (1973).
- [3] V. V. CHKALOVA, V. S. BONDARENKO, G. O. FOKINA and F. N. STRIZHEVSKAYA, *Bull. Acad. Sci. USSR, Phys. Ser.* **35**, 1712–1715 (1971).
- [4] R. A. GRAHAM, *J. Appl. Phys.* **48**(6), 2153–2163 (1977).
- [5] C. S. HARTMANN, SHEN JEN, M. A. DOMALEWSKI, and J. C. ANDLE, Improved accuracy for determining SAW-transducer capacitance and κ^2 . In *Ultrasonics Symposium*, pp. 161–167. IEEE (1987).
- [6] G. KOVACS, G. TRATTNIG and E. LANGER. Accurate determination of material constants of piezoelectric crystals from SAW velocity measurements. In *Ultrasonics Symposium*, 269–272. IEEE (1988).
- [7] E. LANGER, S. SELBERHERR and P. A. MARKOWICH, Surface and bulk wave velocities in arbitrary anisotropic piezoelectric materials. In *Ultrasonics Symposium*, 1157–1160. IEEE (1983).
- [8] E. LANGER, S. SELBERHERR, P. A. MARKOWICH and C. A. RINGHOFER, Numerical analysis of acoustic wave generation in anisotropic piezoelectric materials. In *Ultrasonics Symposium*, 350–353. IEEE (1982).
- [9] W. R. MADER and H. R. STOCKER, Extended impulse model for the design of precise SAW filters on quartz. In *Ultrasonics Symposium*, 29–34. IEEE (1982).
- [10] R. F. MILSOM, J. HEIGHWAY, N. H. C. REILLY and M. REDWOOD, Comparison of exact theoretical predictions and experimental results for interdigital transducers. In *Ultrasonics Symposium*, 406–411. IEEE (1974).
- [11] Y. NAKAGAWA, K. YAMANOUCHI and K. SHIBAYAMA, *J. Appl. Phys.* **44**(9), 3969–3974 (September 1973).
- [12] R. D. RICHTMYER and K. W. MORTON, *Difference Methods for Initial Value Problems*. Interscience, New York (1967).
- [13] A. J. SLOBODNIK, E. D. CONWAY and R. T. DELMONICO, *Microwave Acoustics Handbook*. U.S. AFCL *Phys. Sci. Res. Pap.* **1A**, 27–28 (1973).
- [14] R. T. SMITH and F. S. WELSH, *J. Appl. Phys.* **42**(6), 2219–2230 (May 1971).
- [15] A. W. WARNER, M. ONOE and G. A. COQUIN, *J. Acoust. Soc. Am.* **42**, 1223–1231 (1967).

(Received 10 November 1989; received for publication 3 September 1990)